Transient freezing-thawing phenomena in water-filled cohesive porous materials

Teddy Fen-Chong * Antonin Fabbri Aza Azouni

Institut Navier, LMSGC, 2 allée Kepler - 77420 Champs-sur-Marne, France

---

Abstract

An oscillator circuit-based capacitive method is used to study the ice/water phase transition in cohesive porous materials like water-filled fused glass beads. It straightforwardly gives the temperature domain of supercooling, freezing, and melting. It also provides an estimation of the ice content time-evolution during the transient stage of solidification and melting. This is done through calibration tests at 20^oC on a progressively dried sample and through an up-scaling dielectric model. The latter allows to take account of the temperature and frequency dependence of the water dielectric constant as well as the slight difference between the dielectric constants of water vapour ($\simeq 1$) and ice ($\simeq 3.2$). From the ice content-versus-time curve, the water-to-ice phase transition dynamics is found to follow the Avrami law, the exponent of which is close to 0.5. This suggests that the ice/liquid interface is planar so that the liquid and ice pressures are equal, which is confirmed through the Gibbs-Thomson and Young-Laplace equations. The resulting pore pressure can then be predicted in the framework of linear poroelasticity. The analysis reveals a three-step time-history pressure: an increase at the onset of stable ice nuclei, then a relaxation induced by unfrozen water Poiseuille-type flow followed by a further rise until the end of crystallization. In all cases, the pressurization remains very low (0.1 MPa) at the 0^oC-isothermal transient stage of solidification.

Preprint submitted to Elsevier Science *2 September 2005*

Key words: undercooling, ice growth, dielectric, homogeneisation, Lichtenecker, poromechanics, liquid flow

1 Introduction

Most civil engineering or geotechnical durability problems involve water inside porous media, either in unconsolidated form like soils or in cohesive form like stones and cementitious materials. In case of freezing and thawing, the in-pore ice/water phase change behaviour plays a key role (Scherer, 1993; Coussy, 2005; Coussy and Fen-Chong, 2005) through the coupling of the unfrozen water (or ice) content, the pore pressure, the liquid water flow in the porous network, and the thermomechanical behaviour of each porous material constituents. The understanding of such physical phenomena can be improved with the use of an oscillator circuit-based capacitive apparatus.

Like the time domain reflectometry technique (Zakri and Laurent, 1998), the dielectric capacitive method exploits the high permittivity disparity between liquid water and ice, air, or mineral substrate in the radio-frequency range. It practically relies on the variation of the sample capacitance or dielectric constant under drying where in-pore liquid/vapour phase change takes place, and under freezing/thawing where in-pore liquid/ice phase transition occurs. Its ability to characterize water-filled cohesive porous media like stones or cementitious materials under freezing and thawing, was laid out in the previous

---

* Corresponding author
Email addresses: `teddy.fen-chong@lcpc.fr` (Teddy Fen-Chong), `antonin.fabbri@lcpc.fr` (Antonin Fabbri), `aza.azouni@lcpc.fr` (Aza Azouni).

papers (Fen-Chong et al., 2004; Fen-Chong and Fabbri, 2005; Fabbri et al., 2005). In these works, each system was studied after stable thermodynamic equilibrium had been reached.

This paper deals with the transient stage of freezing during which ice crystals grow at the expense of adjacent unfrozen water at 0^oC. Focus is then laid on the in-pore ice content time-evolution (at constant temperature) and on the resulting pressure in the porous network. To do so, the spectroscopic-like dielectric capacitive method is first recalled (section 2) and applied to home-made fused glass beads (section 3). Some features of the so-obtained results are also commented and then expressed in terms of ice saturation degree (section 4), which allows to identify a possible ice growth mechanism. In the last section 5, the pressure is calculated within the well-established poromechanics framework (Coussy, 2004) as in (Coussy and Fen-Chong, 2005; Coussy, 2005). Note that the temperature and ice content (or liquid content) are here assumed to be uniform throughout a tested sample.

For the sake of clarity, in all that follows the term "water" alone refers to the H_2O matter whichever its actual physical state. Conversely the terms "liquid", "vapour", or "ice" specify that water is in its liquid, gaseous, or ice Ih form respectively, while the terms "solid" and "matrix" refer to the backbone constituent of the porous material. At last, the temperature T is always in Kelvin degree when appearing in mathematical expressions while it can be numerically expressed in Celsius degree for engineering conveniency.

2 Dielectric capacitive method

2.1 Basic measurement principle

The local spatial redistribution of polarised electrical charges in a material sample under an applied electric field is characterised by its dielectric constant (dielectric permittivity relative to that of free space) $\varepsilon^* = \varepsilon - j\,\varepsilon_r$, where $j^2 = -1$. The real part ε relates to the behaviour of an ideal insulator and characterises the degree of electric polarisability of the material while the imaginary component ε_r is associated with the electric energy dissipation into heat due to electrical conduction and polarised charges fluctuations.

A capacitive sensor-based apparatus can provide the real part ε via the medium electric capacitance C because:

$$C = \varepsilon\, C_0 \tag{1}$$

in which C_0 is the air electric capacitance for the same geometrical configuration. The capacitive method is well-suited for studying dielectric medium filled with water undergoing phase transition owing to the associated high variation of the water dielectric constant. Since the host medium permittivity ε depends on each constituent permittivity and volume fraction, ε evolves with the content variation of liquid water, as experimentally found or reported in (Eller and Denoth, 1996; Fen-Chong et al., 2004; Fabbri et al., 2005). As regards the liquid/vapour phase change which occurs under drying condition, the water dielectric constant falls from 80.2 (liquid) down to 1 (vapour) (Lide, 2001). The situation is essentially the same for the liquid/ice phase transition that occurs under freezing and thawing condition, as detailed below.

2.2 Temperature and frequency dependence of water permittivity

The water dielectric behaviour is well described by the single relaxation time-based Debye model (Auty and Cole, 1952; Johari and Whalley, 1981; Ellison et al., 1996; Kaatze, 1997; Petrenko and Whitworth, 1999). This means that the real dielectric constant ε_q of ice ($q = i$) and liquid water ($q = \ell$) is given by:

$$\varepsilon_q(\nu, T) = \varepsilon_q^\infty(T) + \frac{\varepsilon_q^s(T) - \varepsilon_q^\infty(T)}{1 + \Big(2\,\pi\,\nu\,\tau_q(T)\Big)^2} \tag{2}$$

where ν is the electric field frequency (in Hz), T the temperature (in K), $\varepsilon_q^s(T) = \varepsilon_q(\nu \to 0, T)$ and $\varepsilon_q^\infty(T) = \varepsilon_q(\nu \to \infty, T)$ are respectively the limiting low-frequency (static) and the limiting high-frequency real dielectric constants of each phase q. In the radio-frequency range, the experimental values of ε_q^s and ε_q^∞ are: $\varepsilon_i^\infty \simeq 3.2$ from 253 K to 272 K (Evans, 1965; Johari and Whalley, 1981; Petrenko and Whitworth, 1999), $\varepsilon_i^s(T) \simeq \varepsilon_i^\infty + \frac{24620}{T-6.2}$ from 133 K to 272 K (Johari and Whalley, 1981), $\varepsilon_\ell^\infty \simeq 5.7$ in average between 273 K and 298 K (Kaatze, 1997), $\varepsilon_\ell^s(T) \simeq 87.8e^{-0.0046(T-273.15)}$ (Ellison et al., 1996; Kaatze, 1997) from 373 K down to 238 K (Ellison et al., 1996). In (2), τ_q is the relaxation time of the electric dipole moments of water molecules in the q-form. It is given by:

$$\tau_q = \tau_q^0\, e^{\frac{-\Delta H_q}{R\,T}} \tag{3}$$

where ΔH_q is the activation enthalpy corresponding to one hydrogen bond, τ_q^0 is a time constant and $R = 8.3147$ J/(K.mol) is the ideal gas constant. From experimental literature data ((Auty and Cole, 1952) for ice and (Kaatze, 1997) for liquid water) we find the following fitted values $\Delta H_i \simeq 54525$ J/mol, $\tau_i^0 \simeq 8.39^{-16}$ s, $\Delta H_\ell \simeq 19775$ J/mol and $\tau_\ell^0 \simeq 2.87^{-15}$ s. It must be stressed out that we have extrapolated the experimental relaxation time data for supercooled water down to -40 ^{o}C.

Under this hypothesis, from 1 MHz to 1 GHz the real dielectric constant of ice is equal to its optical value (electronic polarisation) of $\varepsilon_i^\infty = 3.2$ whereas that of liquid water is still equal to its static value (orientation polarisation) ε_ℓ^s between 80 and 105 depending on the temperature, see figure 1 in (Fabbri et al., 2005). To better show how these temperature dependent permittivities can be useful in estimating the ice content inside a water-saturated material, we now turn to describing the experimental procedure principle.

2.3 Experimental procedure principle

The important point is that the liquid content amount cannot be directly measured by weighing under freezing and thawing conditions: if the material is perfectly isolated, the total mass of water remains constant whereas the mass fractions of ice and liquid vary as the phase change goes on. The only measurable physical quantities are the temperature $T(t)$ and the sample dielectric constant $\overset{*}{\varepsilon}(t)$ histories during freezing and thawing. It is not possible to directly get the liquid water content $S_\ell(t)$ evolution with the temperature.

To do so, we have chosen to measure the sample dielectric constant $\hat{\varepsilon}$ evolution with the liquid water amount S_ℓ under drying at 20 ^{o}C. In this way the liquid water mass varies through the liquid/vapour phase change occurring inside the pores, which can be measured by weighing. This eventually allows to identify an appropriate dielectric homogeneisation modelling (Zakri et al., 1998; Cosenza et al., 2003; Fen-Chong et al., 2004; Bittelli et al., 2004) to represent the role of each constituent permittivity and volume fraction on the host material permittivity:

$$\hat{\varepsilon} = \mathcal{H}\Big(\varepsilon_v, \phi_v; \varepsilon_\ell, \phi_\ell; \varepsilon_m, \phi_m\Big) \tag{4}$$

where ϕ_q denotes the volume ratio of the q-constituent: $q = v$ for the water vapour phase, $q = \ell$ for the liquid water phase and $q = m$ for the solid matrix. The liquid content S_ℓ can be evaluated from the volume fractions ϕ_q, the latter being measured by weighing. The function $\mathcal{H}$ allows to relate the measured macroscopic permittivity $\hat{\varepsilon}$ under drying condition with those (ε_q) acting at the microscopic level. In (4) the microstructural information is implicitly taken into account by the up-scaling model $\mathcal{H}$.

If the microstructural configuration of the different constituents of the host material is assumed to be identical in freezing/thawing and in drying tests, then the same function $\mathcal{H}$ can be used to estimate the liquid content S_ℓ under freezing/thawing condition from the measured $\overset{*}{\varepsilon}(T)$:

$$S_\ell = \mathcal{H}^{-1}\Big(\varepsilon_i; \varepsilon_\ell; \varepsilon_m, \phi_m; \overset{*}{\varepsilon}\Big) \tag{5}$$

in which ε_i substitutes for ε_v to distinguish ice/liquid from vapour/liquid phase changes. Note that no mechanical effect is considered in equations (4) and (5) since ϕ_m is assumed constant and each ε_q only depends on the temperature and the frequency.

3 Experiments

3.1 Materials

Fused glass beads are made from commercial CENTRAVER (now CVp) soda-lime (silica) glass powders which are between 62 to 87 μm in diameter. The as-received materials are poured into a female mould which is then heated in an oven at 630 ^{o}C. In this way the beads collapse and fuse together to yield a cohesive porous medium as shown on the left hand-side of figure 1: the porous network appears as the darker phase (from Scanning Electron Microscopy at LCPC, Paris). Its apparent density is about 1.5 g/cm^3, the mineral density about 2.5 g/cm^3, and its porosity ϕ_0 is 0.40 ± 0.03. The right hand-side of figure 1 shows the pore diameter distribution obtained from mercury injection measurements. Initially it is mainly monodispersely centred around 30 μm with precious few pores about 7 μm. After one freezing and thawing cycle, this distribution almost remains unchanged. One can only note that the initial 7 μm-pores have merged into 10 μm-pores and that the proportion of 100 μm-pores seems to have risen a little. However the inaccuracy associated with mercury injection measurements does not allow to conclude that the porosity has significantly changed.

Cylindrical samples of 50-mm mean diameter and 20-mm mean thickness were used for the drying and freezing/thawing tests; their mean porous space volume is thus about 15.7 cm^3 for a sample volume of 39.3 cm^3. One of them was drilled to insert a T-type thermocouple and to get the sample temperature history for a given imposed temperature time-evolution.

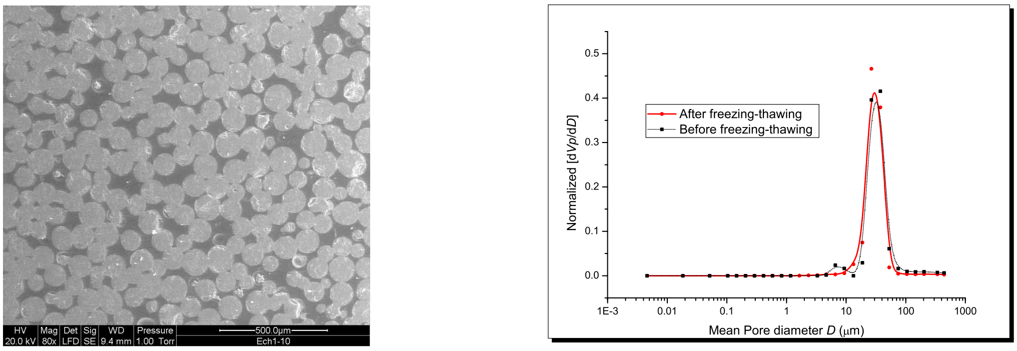

Fig. 1. Fused glass beads microstructure.

Each porous material sample is cleaned up from scraps, dried at 50 ^{o}C in an oven for 3 days before weighing. It is then filled with degased home-made distilled water at 3 kPa air pressure at approximately 20 ^{o}C. However some residual air can be trapped in the sample such that the maximum initial degree saturation can be as low as 0.95 (when comparing the weighed masses and the calculated mass of water that could completely fill the porous space volume obtained from porosimetry measurements). Different water degree saturations are then achieved by using an oven at 50 ^{o}C. Then the sample is rapidly transferred into the capacitive electrodes, wrapped in a Parafilm sheet and tested. Weighing is realised just before and after each capacitive test to evaluate the water mass content and to check that no significant water loss happened.

3.2 Experimental equipment

Each sample is inserted between two plane and circular stainless steel electrode plates of 60 mm diameter. All of them are connected to a 30 MHz-50 MHz oscillator electronic device, which forms an oscillating electric circuit at the resonant frequency $\tilde{\nu}$, see figure 1 of (Fen-Chong et al., 2004) and figure 2 of (Fabbri et al., 2005). This device, designed and manufactured by the

"Centre d'Études et de Construction de Prototypes" at Rouen (France), was implementing a frequency divider (5632) in order to reach a low frequency range (in the order of several kHz) before transmitting the signal to a digital storage oscilloscope TDS1002 TEKTRONIX (for signal-shape check) and to a multifunction counter-timer 34907A AGILENT. The experimental apparatus delivers the reduced resonant frequency $F = \frac{\tilde{\nu}}{5632}$ that depends on the actual capacitance of the dielectric sample. In all that follows, the term "frequency" alone will be used.

The sample temperature is imposed by a Galden PFPE HT200 cryogenic fluid (from SOLVAY SOLEXIS) which circulates from a computer-controlled HÜBER cryostat. This fluid was chosen for its low static dielectric constant (about 2 at 20 ^{o}C) and because it does not disturb the frequency answer of the apparatus during freezing and thawing. This problem was met with ethanol as formerly used in (Fen-Chong et al., 2004) for isothermal tests at 20 ^{o}C.

As a preliminary stage, different commercial ceramic capacitors connected in parallel to different commercial resistors were directly plugged to the oscillator electronic device that was isolated from the other apparatus parts in this case. This is done to check if the ionic conduction-induced dielectric loss (part of the resistive term ε_r) of the non-ideal insulator porous materials does not influence the frequency measures. This is found to be true for capacitance values ranging from 1 to 47 pF, thus giving the capacitance operation range of our oscillator device.

3.3 Calibrations

Calibration tests were conducted to obtain the relation between F and the sample capacitance C, as described in (Fabbri et al., 2005). The following affine relationship was found:

$$C \simeq 113.6 - 0.018\, F. \tag{6}$$

This calibration curve provides a means of converting F into the sample capacitance C and thus its real dielectric constant through (1), either under drying condition ($\hat{\varepsilon}$) or freezing/thawing condition ($\overset{*}{\varepsilon}$).

Drying tests were then conducted to obtain the relation between the liquid water content and the frequency F. Liquid water content or amount is here expressed as the liquid water saturation degree $S_\ell = \frac{\phi_\ell}{\phi_0}$ (ratio of liquid volume fraction over the sample initial porosity, which is also the ratio of the liquid-filled volume over the initial porous space volume) and measured by weighing. The as-obtained results are eventually turned into a $\hat{\varepsilon}(S_\ell)$ calibration curve through (1) and (6), which yields:

$$\hat{\varepsilon} \simeq 2.9 + 13.8\, S_\ell \qquad \text{for fused glass beads.} \tag{7}$$

Affine-type $\hat{\varepsilon}(S_\ell)$ relation was also found for cement paste, calcareous Caen stones, and soils, as experimentally found or reported in (Fen-Chong et al., 2004; Fabbri et al., 2005); it is also nearly the case for soils in (Eller and Denoth, 1996).

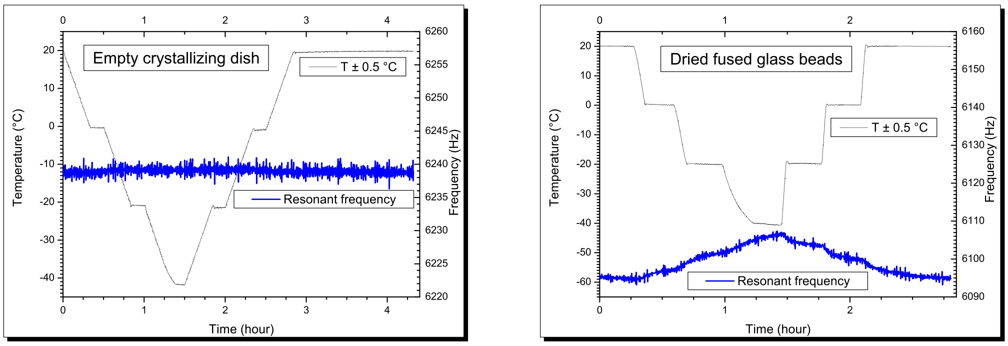

Fig. 2. Temperature independence of the frequency of the capacitive experimental device. The fused glass beads sample may have contained little residual water, which is of no significance as regards the frequency experimental uncertainty (±5 Hz).

3.4 So-obtained results in freezing/thawing

3.4.1 Temperature independence of the solid skeleton permittivity

First we ensured that, in the absence of liquid water in the volume comprised between the stainless steel electrode plates, the experimental apparatus does not provide a frequency F varying with the temperature. Figure 2 shows that this condition is well fulfilled for an empty crystallizing dish.

Then the temperature dependence of the solid constituent permittivity ε_m of fused glass beads was examined. Figure 2 shows that the frequency remains nearly constant for a dried fused glass beads sample submitted to freezing and thawing. The slight F variation probably comes from little residual water, which nevertheless remains inside the frequency experimental uncertainty domain (±5 Hz). The latter was determined by repeating the same test on the same sample of each kind of several water-filled materials (fused glass beads, calcareous Caen stone, crystallizing dish, sandstone, cement). In the end, it can be concluded that ε_m is independent of the temperature.

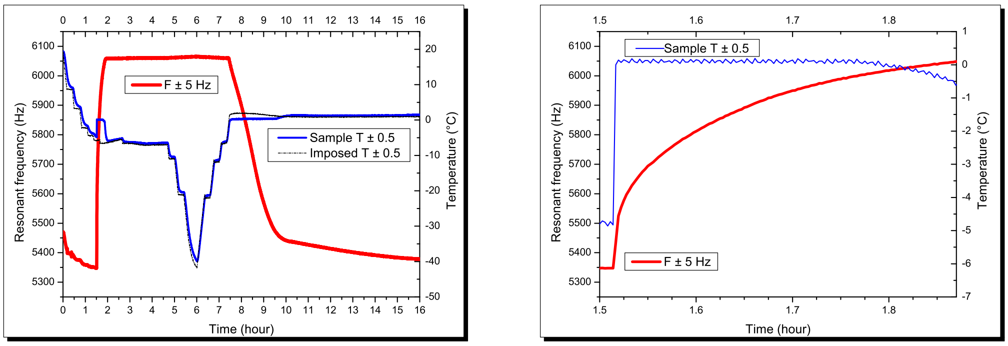

Fig. 3. Freezing and thawing fused glass beads: frequency time-variation. The onset of freezing is about -5°C and the melting temperature is about 0°C.

It was also checked that wrapping a sample by the Parafilm sheet is dielectrically negligible and that the experimental apparatus behaviour is not influenced by all nearby electric appliances.

3.4.2 Frequency evolution of frozen/thawed fused glass beads

Figure 3 shows the frequency time-evolution with that of the temperature for the water-saturated fused glass beads sample. The temperature at which ice formation begins is $T_s \simeq -5$ ^{o}C when both temperature and frequency starts increasing: T_s is associated with the end of water supercooling. Shortly after, the temperature remains constant at 0 ± 0.5 ^{o}C for $\Delta t \simeq 21$ min while the frequency goes on rising. The frequency gets stable at $\Delta t \simeq 30$ min, which gives the end of crystallization. Note that between $\Delta t \simeq 21$ min and $\Delta t \simeq 30$ min, the temperature drops from $\simeq -0.5$ to $\simeq -6$ ^{o}C. On heating the in-pore ice melting occurs when the temperature gets constant and equal to 0 ± 0.5 ^{o}C while the frequency decreases slowly because of ice changing into liquid water.

Indeed the behaviour of the in-pore water of these fused glass beads is found to mimic that of bulk water contained in crystallizing dishes. Here the temperature at which crystallization begins is about -6 ^{o}C nearly the same as for fused glass beads. On the other hand, solidification is much slower than for fused glass beads since here it lasts over $t \simeq 1$ h $\frac{1}{4}$. This comes from the greater amount of water contained in a 47-ml Schott Duran crystallizing dish than in our fused glass beads samples. The same kind of behaviour was observed during freezing in water-filled pipes occurring at the end of water supercooling (Akyurt et al., 2002). We now turn to determining the ice content time-evolution inside each sample.

4 Data analysis

4.1 Choice of a micro-macro dielectric model

An affine experimental $\hat{\varepsilon}(S_\ell)$ curve was found for fused glass beads under drying condition. To recover an expression like (7) for the whole range of S_ℓ and ϕ_0 values (between 0 and 1) while knowing the role of the microstructure and of each constituent permittivity and volume fraction on the host material permittivity, use can be made of the self-consistent scheme-based Lichtenecker model (Zakri et al., 1998). The derivation of the Lichtenecker affine form is given in (Fabbri et al., 2005) and, in particular, assumes that no particular pore shape nor orientation is privileged with regard to the direction of the external electric field, which is consistent with the microstructure shown in figure 1. For the case at hand, it writes as:

$$\varepsilon = \varepsilon_m^{1-\phi_0} \left(S_\ell \, \varepsilon_\ell^{\phi_0} + (1 - S_\ell) \, \varepsilon_{n\ell}^{\phi_0} \right) \tag{8}$$

where $\varepsilon_{n\ell}$ refers to a non-liquid form of water (ice or vapour). Since the water vapour dielectric constant $\varepsilon_v = 1$ for temperatures ranging from 0 ^{o}C to 100 ^{o}C (Lide, 2001), for the drying tests (8) becomes ($\varepsilon_{n\ell} \equiv \varepsilon_v$):

$$\hat{\varepsilon} = \varepsilon_m^{1-\phi_0} \left(\left(\varepsilon_\ell^{\phi_0} - 1 \right) S_\ell + 1 \right) \tag{9}$$

as a particular relation (4) for our porous materials. For fused glass beads, comparison between (7) and (9) yields $\varepsilon_m \simeq 5.9$ and $\varepsilon_\ell \simeq 79.6$ at 20 ^{o}C, which agrees with the values found in another way (Fabbri et al., 2005).

4.2 Ice content estimation

Under freezing and thawing condition, (8) is inverted with $\varepsilon_{n\ell} \equiv \varepsilon_i$, such that the relation (5), here expressed in terms of the ice saturation degree S_i ($S_i = 1 - S_\ell$), takes the particular form of:

$$S_i = 1 - \left(\frac{\overset{*}{\varepsilon}}{\varepsilon_m^{1-\phi_0}} - \varepsilon_i^{\phi_0} \right) \left(\varepsilon_\ell^{\phi_0} - \varepsilon_i^{\phi_0} \right)^{-1} \tag{10}$$

where $\overset{*}{\varepsilon}(T)$ is determined through (1), (6), and the frequency delivered by the capacitive apparatus as the temperature T varies. Note that the derivation of (10) requires to presume that both porous network and solid matrix volumes remain constant.

With the determined values of the solid matrix permittivity ($\varepsilon_m \simeq 5.9$) and the porosity ($\phi_0 \simeq 0.40$) of our porous material, the temperature and frequency dependence of the liquid water permittivity (see section 2.2), the frequency and temperature time-evolution during a freezing/thawing test (see figure 3), the ice content can be straightforwardly predicted from (10), as shown in figure 4. Note that the porosity is considered constant in this procedure: as

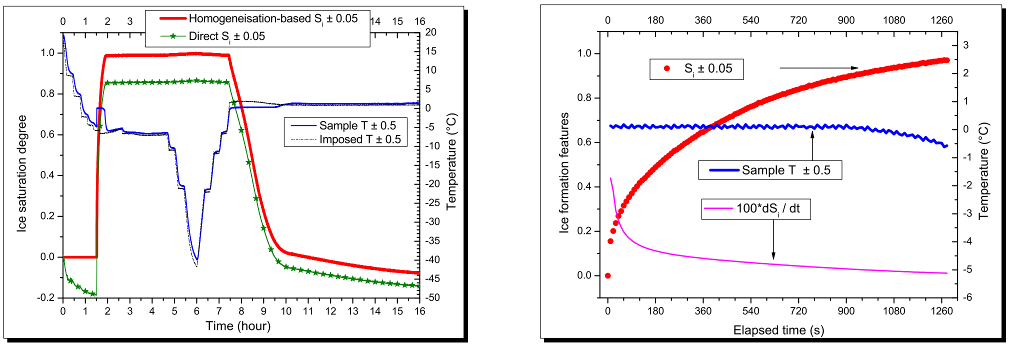

Fig. 4. Freezing and thawing fused glass beads: time-evolution of ice content.

shown in the right hand-side of figure 1, the pore size distribution almost remains unchanged after one freezing/thawing cycle.

Figure 4 shows the thermal and ice content time-evolution in fused glass beads on freezing and thawing. It depicts the same ice/water phase change as discussed in section 3.4.2. It also shows the direct estimation of the ice saturation degree without use of any up-scaling dielectric approach like the Lichtenecker model. In such way, both drying and freezing/thawing tests simply provide the dependence of the liquid water amount on the temperature by eliminating the resonant frequency parameter from the $F(S_\ell)$ curve in drying and the $F(T)$ curve in freezing/thawing. Such data analysis surmises that both the slight difference between the dielectric constants of air (1) and ice (3.2), as well as the temperature and frequency dependence of the water dielectric constant, are of no importance. This is not the case since the so-predicted ice content varies before any crystallization occurs $(0 \leq t \leq 1 \text{ h } \frac{1}{2})$, can go down as low as -0.2 (well above the uncertainty error of -0.05), and underestimates the highest ice content (0.87 instead of 0.99).

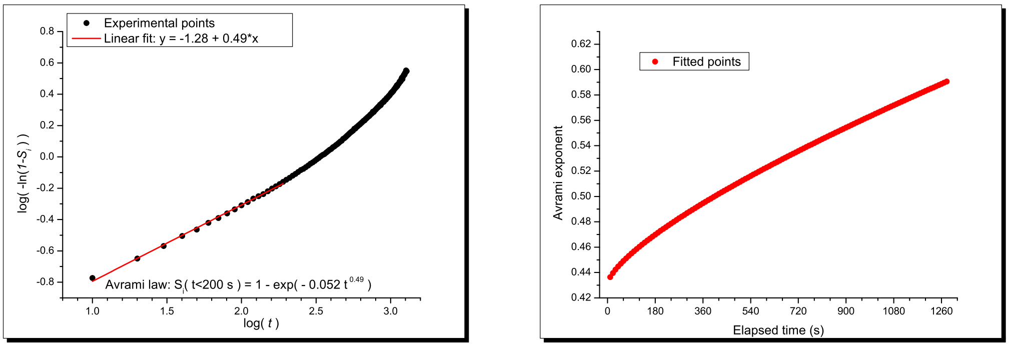

Fig. 5. Freezing fused glass beads: analysis of the ice growth mechanisms.

4.3 Mechanism of ice formation in fused glass beads

The water-to-ice phase transition results from ice germs nucleation and from the already stable ice crystals growth, both at the expense of the remaining liquid water. One simple, though physically founded, way of describing this in-pore ice formation relies on the Avrami law (Papon et al., 2002):

$$S_i = 1 - \exp(-\lambda\, t^n) \tag{11}$$

where λ is a constant and n is the Avrami exponent that characterizes the new phase growth mode. This law assumes a time-dependent nucleation rate and takes account of the fact that the initially isolated ice crystals end up in coalescing due to steric hindrance. The Avrami exponent can be identified if the $S_i(t)$ curve can be recast in the following affine form: $\log(-\ln(1 - S_i)) = \log \lambda + n\, \log t$. The left hand-side of figure 5 shows that the onset of crystallization obeys to the Avrami law. The Avrami exponent n is fitted to be 0.49 for a freezing time less than 200 s:

$$S_i = 1 - \exp(-0.052\, t^{0.49}). \tag{12}$$

The same procedure for $S_i \pm 0.05$ yields the miminum and maximum Avrami exponents of 0.44 and 0.57.

Although the $\log(-\ln(1 - S_i))$-$\log t$ curve is no more affine for freezing time over 200 s, it is possible to assume that the Avrami law is still followed by allowing the Avrami exponent to vary with time. Doing so, it is found that:

$$n(t \geq 0) = 0.43 + \frac{0.001}{\log t}\Big(\exp(2\log t) - 1\Big) \tag{13}$$

where t is expressed in s. The time-evolution of $n(t)$ during the freezing stage is plotted in the right hand-side of figure 5. One can see that the Avrami exponent remains between about 0.44 and 0.62 and thus in the order of 0.5.

Finally, from (12) and (13), the ice content curve can be expressed as:

$$S_i(t) = 1 - \exp\Big(-0.052\, t^{\left(0.43 + \frac{0.001}{\log t}(\exp(2\log t) - 1)\right)}\Big) \tag{14}$$

for the crystallization period (right hand-side of figure 4). The ice saturation degree rate is found to be initially about 0.0044 s^{-1}. Since S_i is the ratio of the current ice-filled volume over the initial porous space volume, for our given material (see data in section 3.1) the initial ice volume growth time rate is about 0.07 cm^3/s. As can be seen on the right hand-side of figure 3, the ice saturation degree rate is highest at the onset of freezing and then decreases quickly down to 0. Hence it is reasonable to assume that each constituent of the fused glass bead sample undergoes infinitesimal transformations as regards all mechanical and thermodynamical phenomena.

4.4 Discussion

In all cases, our Avrami exponent is close to 0.5 which corresponds to planar ice crystals growths controlled by molecular diffusion from the liquid state to the nucleating icy sites (Papon et al., 2002). This kind of ice formation is also reported in (Akyurt et al., 2002) under the form of dendritic ice consisting of thin plate-like crystals interspersed in liquid water during the first 30 seconds.

The fact that the ice/liquid water interface tends to be planar can be explained as follows. First we recall that the pressure p_i inside an ice crystal of mean curvature κ^* in mechanical equilibrium with neighbouring liquid water at the pressure p_ℓ is governed by the Young-Laplace relation:

$$p_{cap} = p_i - p_\ell = \gamma\,\kappa^* \tag{15}$$

where γ is the water/ice interface energy and p_{cap} is the so-called capillary pressure. Assuming that the ice/water phase change takes place as a non-dissipative process and that temperature drops are not too large in order to neglect the quadratic terms related to the water compressibility and to the thermal expansion, the transition temperature T^* of this two-phase system is approximated by (Coussy, 2005):

$$p_{cap} = S_f\,(T_m - T^*) \tag{16}$$

where S_f is the entropy of fusion per unit of crystal volume. In (15) and (16), the reference state is defined at atmospheric pressure ($p_i = p_\ell = 0$) and $T = T_m = 0\ {}^o$C. From (15) and (16) the well-known Gibbs-Thomson equation is recovered:

$$T_m - T^* = \frac{\gamma\,\kappa^*}{S_f} \tag{17}$$

As shown in figure 4, $T^* \simeq T_m = 0$ ^{o}C for $\Delta t \simeq 21$ min: (17) implies that $\kappa^* \simeq 0$, which means that the ice/liquid water interface curvature tends to be planar and thus supports our experimentally found Avrami exponent value in the order of 0.5. From (16), this also indicates that ice and liquid water are almost at the same pressure. The latter can be evaluated from the determined ice content-versus-time function (14), which is going to be worked out.

5 Application: from ice content to pore pressure estimation

5.1 Closed pores

Consider a solid matrix embedding a water-filled porous volume of arbitrary geometrical form. From $t = 0$, this system is submitted to freezing according to (14). Its initial porosity is ϕ_0 and its actual one is ϕ. We consider the whole system to be at $T_m = 0$ ^{o}C during the whole crystallization process, such that the liquid and ice pressures are imposed identical: the pore pressure remains uniform within the closed pore in all the following.

In accordance with linear isotropic elasticity, the relative pore volume change $\frac{\phi-\phi_0}{\phi_0}$ is related to the pore pressure p_{max}, the ice content S_i, and the pore bulk modulus K_p by:

$$\frac{\phi - \phi_0}{\phi_0} = \left(\frac{\rho_{\ell_0}}{\rho_i} - 1\right) S_i - \frac{p_{max}}{K_p} \tag{18}$$

The first term of the right hand-side accounts for the relative pore volume variation accompanying the mass density change when liquid water solidifies freely (without any stress constraint), and the second one for the mechanical response of the surrounding matrix. In (18), the initial state is defined at atmospheric pressure ($p = 0$) and $T = T_m$. In this configuration, $\rho_{\ell_0} = 0.9998$ g/cm^3 and $\rho_{i_0} = 0.9167$ g/cm^3 are the liquid water and ice mass densities (Petrenko and Whitworth, 1999), while the actual ice mass density ρ_i can here be linearized as (Coussy, 2005):

$$\frac{\rho_{i_0}}{\rho_i} \simeq 1 - \frac{p_i}{K_i} \tag{19}$$

where K_i is the ice bulk modulus and the temperature is assumed constant (and thus equal to T_m). From (18) and (19) and recalling that $p_i = p_\ell$:

$$p_{max}(t) = \frac{\left(K_p(t)\left(\frac{\rho_{\ell_0}}{\rho_{i_0}} - 1\right)S_i(t) - \left(\frac{\phi-\phi_0}{\phi_0}\right)\right)}{1 + \frac{K_p(t)}{K_i}\frac{\rho_{\ell_0}}{\rho_{i_0}}S_i(t)}. \tag{20}$$

Because the ice-to-liquid ratio varies in the pore, its bulk modulus K_p evolves with time. It is evaluated in (20) by presuming that the pore content can be replaced by a fictitious homogeneous medium behaving globally in the same way (Zaoui, 2002). Here use is made of the well-known Hashin-Shtrikmann bounds. When the spatial distribution of each phase is isotropic, these bounds are the optimized ones if only the volume fractions, the bulk moduli (K_q), and shear moduli (G_q) of each phase (q) are known. In the case at hand,

$$K_p^+ = K_i + \frac{(K_\ell - K_i)(3K_i + 4G_i)}{(3K_i + 4G_i) + 3(K_\ell - K_i)S_i}(1 - S_i) \tag{21}$$

$$K_p^- = K_\ell + \frac{(K_i - K_\ell)(3K_\ell + 4G_\ell)}{(3K_\ell + 4G_\ell) + 3(K_i - K_\ell)(1 - S_i)}S_i. \tag{22}$$

According to (Kleinberg and Griffin, 2005), ice forms preferentially in the center of the pores, leaving the unfrozen water in contact with the solid pore wall. In this case, the stiffer phase (ice) is likely to be embedded in the softer one (liquid water) such that the lower Hashin-Shtrikmann bound given by (22) should provide an estimation of the pore bulk modulus.

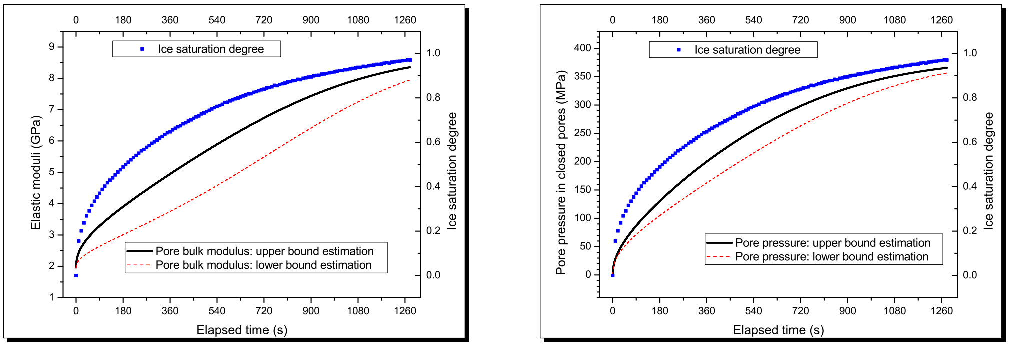

Fig. 6. Freezing fused glass beads: pore bulk modulus time-evolution (left); closed pore pressure time-evolution (right).

The left hand-side of figure 6 shows the time-variation of K_p during the freezing stage. Both bounds vary from the value of $K_\ell = 1.96$ GPa (Speedy, 1987) to almost $K_i = 8.74$ GPa (Petrenko and Whitworth, 1999). The latter is not completely reached since $S_i < 1$ experimentally. In (21) and (22), we also put $G_i = 3.46$ GPa (Petrenko and Whitworth, 1999) and $G_\ell = 0$. All liquid and ice parameter values are taken at 0 ^{o}C. The resulting pressure p_{max} is then found to increase quickly to more than 370 MPa at constant porosity $\phi = \phi_0 = 0.40$, as shown in the right hand-side of figure 6. Such value is not surprising since (20) is derived for a closed pore but is clearly excessive since no damage can be detected in the sample (see for instance the right hand-side of figure 1). Even if the pore volume is allowed to vary, similar, though lower, values are however obtained from the complete set of equations of poroelasticity (Coussy, 2004).

One way of overcoming this difficulty consists in taking account of liquid flow through the porous network. Indeed some residual air can be trapped in the sample during the experimental saturation stage: the existence of such compressible air is not meaningless since it can serve as interspersed escape boundaries for water flows during the crystallization stage.

5.2 Open porous network

We consider that the fused glass beads microstructure can be represented as a set of big pores of radius R connected to each other through n smaller cylindrical pores of radius r_0 and length L. Liquid flow is allowed to occur in these channel-like pores. On freezing the effective radius r through which liquid water can still flow is given by:

$$r = r_0\sqrt{1 - S_i}. \tag{23}$$

Consider now the part of liquid water which was originally contained in the pore before freezing onset and which has transformed into ice at time t. Let $\varphi = \frac{\rho_i}{\rho_{\ell_0}} S_i$ be its actual mass fraction over the initial liquid mass contained in the pore. From (19), this quantity depends on both S_i and p_i: $\varphi = \frac{\rho_{i_0}}{\rho_{\ell_0}} \frac{S_i}{1-\frac{p_i}{K_i}}$. Indeed, with the previous numerical values the term $\frac{p_i}{K_i} \leq \frac{p_{max}}{K_i} \ll 1$, such that φ can be recast in the following linear form:

$$\varphi \simeq \frac{\rho_{i_0}}{\rho_{\ell_0}} S_i. \tag{24}$$

We assume a Poiseuille flow in the channels that separate the pore from surrounding pores remaining at zero liquid pressure. It can then be shown that the liquid mass v flowing from a big pore (per unit of initial liquid mass contained in the pore) is governed by (Coussy and Fen-Chong, 2005)

$$\begin{cases} \Big(1 + \gamma(1 - \varphi)\Big)\frac{\mathrm{d}v}{\mathrm{d}t} + \frac{1}{\tau} v = \frac{1}{\eta}\, p_{max}\, \varphi \\ v(t = 0) = 0 \end{cases} \tag{25}$$

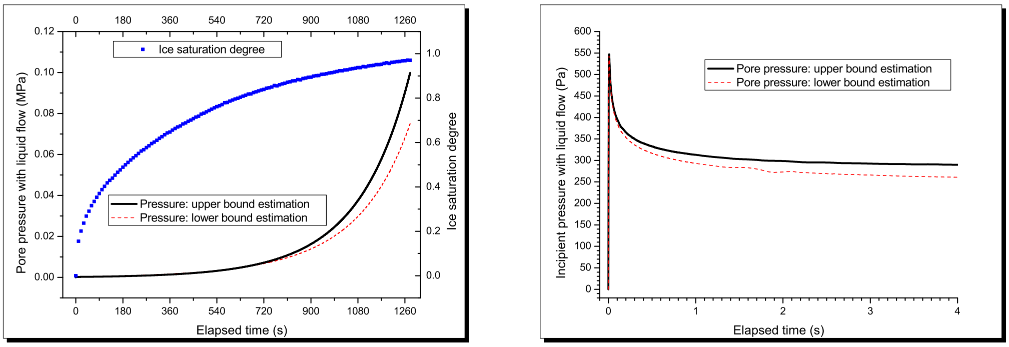

Fig. 7. Freezing fused glass beads: pore pressure when water is allowed to flow from frozen sites to unfrozen ones (left); pore pressurization just after the onset of freezing (right).

where $\gamma = \frac{\frac{1}{K_\ell}-\frac{1}{K_i}}{\frac{1}{\frac{4}{3}G_s}+\frac{1}{K_i}}$, $\eta = \frac{8L\,V}{n\,\pi\,r^4}\eta_\ell$, $\tau = \eta\left(\frac{1}{\frac{4}{3}G_s}+\frac{1}{K_i}\right)$, $V = \frac{4}{3}\pi R^3$, η_ℓ the water dynamic viscosity, and G_s the soda-lima silica glass shear modulus. The pore pressure is eventually given by the Poiseuille equation (recall that $p = p_i = p_\ell$):

$$p = \eta\,\frac{\mathrm{d}v}{\mathrm{d}t} \tag{26}$$

In the following we use the following values: $\eta_\ell = 1.79 \times 10^{-3}$ Pa s, $G_s =$ 30 GPa (Pilkington, 2005), $r_0 \simeq 1$ μm, $R \simeq 30$ μm (see also the fused glass beads microstructure of figure 1), $n = 1$, and $L \simeq 1$ cm .

From (14) and (20)-(26), figure 7 shows how the pore pressure evolves with time during freezing. At the beginning of freezing, it quasi-instantaneously increases up to $\simeq$ 550 Pa before relaxing down to $\simeq$ 250 Pa. From then, the pressure increases again. At $t = 21$ min, the upper-bound pore pressure is about only 0.1 MPa, which cannot damage the material (at least 19 MPa is required (Pilkington, 2005)).

Note also that the Clapeyron equation for ice/water system (Lide, 2001; Papon et al., 2002):

$$P/\mathrm{MPa} = -13.4(T_m - T) + 0.1 \tag{27}$$

provides that for a temperature equal to -0.5^{o}C, the corresponding equilibrium pressure is 6.7 MPa. This shows that our calculated pore pressure is largely in the equilibrium pressure range induced by the experimental temperature variations around 0°C.

6 Conclusion

In this paper we succeeded in determining the ice content time-evolution by use of an oscillator circuit-based capacitive method. From this, we found that the ice formation in fused glass beads follows the Avrami law at the 0°C-isothermal transient freezing stage. The Avrami exponent is estimated to be in the order of 0.5, which indicates that the ice/liquid interface tends to be planar so that the liquid and ice pressures are almost equal. This is confirmed through thermodynamical and mechanical considerations, i.e. the Gibbs-Thomson and Young-Laplace equations. It is worthwhile to note that our results are different from what is observed on cement pastes, soils, glass powder, or vycor (Brun et al., 1977; Béjaoui et al., 2002; Watanabe and Mizogucchi, 2002; Bittelli et al., 2004; Fabbri et al., 2005; Kleinberg and Griffin, 2005). In particular, cementitious materials exhibit interconnected pores of different sizes ranging from 1 nm to 1 mm (unlike our fused glass beads which are mainly monodispersely centred around 30 μm). In this case, progressive freezing temperature depressions from -5 to -50 ^{o}C are commonly encountered, which is attributed to the progressive ice propagation through narrower channel-like pores (interconnecting pores of bigger sizes) (Scherer, 1993): this whole process is then reasonably captured by an equilibrium relation like Gibbs-Thomson (17) and involves curved ice/liquid interfaces. In our case, freezing occurs at the end of in-pore water supercooling and as a transient phenomenon at the quasi-constant temperature of 0 ^{o}C.

In addition, through an elementary poroelastic modelling, we made evident that the pore pressure remains very low (less than 0.1 MPa) at the 0°C-isothermal transient stage of solidification. Since this value is much lower than the reported critical stress, the material is not damaged, which is experimentally observed.

At last, a more refined analysis would require to take account of the system actual complexity (temperature, ice content, permittivity gradients, heat conduction and convection), which is to be tackled in future work.

Acknowledgements

We are indebted to Rémy Di Pasquale (a student from the University Paris VII) for his contribution to the experiments, Philippe Vié for providing and characterizing the fused glass beads samples, and Jérôme Mésière (a student from the Institut Galilée, University Paris XIII) for the micrographs.

References

Akyurt, M., Zaki, G., and Habeebullah, B. (2002). Freezing phenomena in ice-water systems. *Energy Conversion and Management*, 43:1773–1789.

Auty, R. P. and Cole, R. H. (1952). Dielectric properties of ice and solid D_20. *The Journal of Chemical Physics*, 20(8):1309–1314.

Béjaoui, S., Revertégat, E., and Bournazel, J. P. (2002). Mécanismes de formation de la glace au sein des pâtes de ciment et des bétons. *Revue Française de Génie Civil*, 6:1309–1332.

Bittelli, M., Flury, M., and Roth, K. (2004). Use of dielectric spectroscopy to estimate ice content in frozen porous media. *Water Resources Research*, 40:WO4212.

Brun, M., Lallemand, A., Quinson, J. F., and Eyraud, C. (1977). A new method for the simultaneous determination of the size and shape of pores: the thermoporometry. *Thermochimica Acta*, 21:59–88.

Cosenza, P., Camerlynck, C., and Tabbagh, A. (2003). Differential effective medium schemes for investigating the relationship between high-frequency relative dielectric permittivity and water content of soils. *Water Resources Research*, 39(9):1230–1242.

Coussy, O. (2004). *Poromechanics*. John Wiley & Sons.

Coussy, O. (2005). Poromechanics of freezing materials. *Journal of the Mechanics and Physics of Solids*, 53(8):1689–1718.

Coussy, O. and Fen-Chong, T. (2005). Crystallization, pore relaxation and micro-cryosuction in cohesive porous materials. *Comptes Rendus Mecanique*, 333(6):507–512.

Eller, H. and Denoth, A. (1996). A capacitive soil moisture sensor. *Journal of Hydrology*, 185:137–146.

Ellison, W. J., Lamkaouchi, K., and Moreau, J. M. (1996). Water: a dielectric reference. *Journal of Molecular Liquids*, 68:171–279.

Evans, S. (1965). Dielectric properties of ice and snow - a review. *Journal of Glaciology*, 5(42):773–792.

Fabbri, A., Fen-Chong, T., and Coussy, O. (2005). Dielectric capacity, liquid water, and pore structure of thawing/freezing materials. *Cold Regions Science and Technology*, page Accepted.

Fen-Chong, T. and Fabbri, A. (2005). Freezing and thawing porous media : experimental study with a dielectric capacitive method. *Comptes Rendus Mecanique*, 333(5):425–430.

Fen-Chong, T., Fabbri, A., Guilbaud, J. P., and Coussy, O. (2004). Determination of liquid water content and dielectric constant in porous media by the capacitive method. *Comptes Rendus Mecanique*, 332(8):639–645.

Johari, G. P. and Whalley, E. (1981). The dielectric properties of ice Ih in the range 272-133 k. *The Journal of Chemical Physics*, 75(3):1333–1340.

Kaatze, U. (1997). The dielectric properties of water in its different states of interaction. *Journal of Solution Chemistry*, 26(11):1049–1112.

Kleinberg, R. L. and Griffin, D. D. (2005). NMR measurements of permafrost: unfrozen water assay, pore-scale distribution of ice, and hydraulic permeability of sediments. *Cold Regions Science and Technology*, 42:63–77.

Lide, D. R., editor (2001). *Handbook of Chemistry and Physics 2001-2002*. CRC Press, 82nd edition.

Papon, P., Leblond, J., and Meijer, P. H. E. (2002). *The Physics of Phase Transitions: Concepts and Applications*. Springer.

Petrenko, V. F. and Whitworth, R. W. (1999). *Physics of Ice*. Oxford University Press.

Pilkington (2005). *Properties of soda-lime-silica float glass*. Pilkington PLC. http://www.pilkington.com/resources/ats129swproperties20050715.doc.

Scherer, G. W. (1993). Freezing gels. *Journal of Non-Crystalline Solids*, 155:1–25.

Speedy, R. J. (1987). Thermodynamic properties of supercooled water at

1 atm. *The Journal of Physical Chemistry*, 91(12):3354–3358.

Watanabe, K. and Mizogucchi, M. (2002). Amount of unfrozen water in frozen porous media saturated with solution. *Cold Regions Science and Technology*, 34:103–110.

Zakri, T. and Laurent, J.-P. (1998). Time domain reflectometry techniques for water content measurement. In *High Temperatures - High Pressures*, volume 30 of *14 ECTP Proceedings*, pages 397–401.

Zakri, T., Laurent, J.-P., and Vauclin, M. (1998). Theoretical evidence for Lichtenecker's mixture formulae based on the effective medium theory. *Journal of Physics D: Applied Physics*, 31:1589–1594.

Zaoui, A. (2002). Continuum micromechanics: survey. *Journal of Engineering Mechanics*, 128:808–816.